


## More insight on the isothermal spreading of solid MoO<sub>3</sub> into ZSM-5 zeolite

Faouzi Ayari<sup>1,2</sup>  · Emna Mannei<sup>1</sup> · Esther Asedegbega-Nieto<sup>3</sup> · Mourad Mhamdi<sup>1,4</sup> · Antonio Ricardo Guerrero-Ruiz<sup>3</sup> · Gérard Delahay<sup>5</sup> · Abdelhamid Ghorbel<sup>1</sup>

Received: 28 November 2017 / Accepted: 25 January 2018 / Published online: 29 January 2018  
© Akadémiai Kiadó, Budapest, Hungary 2018

**Abstract** Pure MoO<sub>3</sub> undergoes dehydration under helium stream between room temperature and 220 °C before being transformed into MoO<sub>2,87</sub> and lost by evaporation at 650 °C. However, in the presence of NH<sub>4</sub><sup>+</sup>-ZSM-5 zeolite (Mo/Al = 1), the dehydration of the mixture and the deammonization of the zeolite take place below 440 °C. In this water-rich atmosphere, a fraction of MoO<sub>3</sub> is rehydrated and transformed into gaseous MoO<sub>2</sub>(OH)<sub>2</sub> at 220–440 °C instead of being reduced. Despite the significant Mo weight loss, MoO<sub>2</sub>(OH)<sub>2</sub> (g) reacts with ZSM-5 zeolite and is transformed into polymolybdate species upon 4 h of isothermal exchange at 500 °C. However, when the reaction time is prolonged from 4 to 8 h, the residual MoO<sub>3</sub> undergoes an agglomeration before being transformed into mono- and dimolybdate species following 12 h of exchange. The determination of band gap energy by means of the diffuse reflectance spectroscopy allowed the identification of Mo species and the quantification of residual MoO<sub>3</sub> (55% of the total Mo), which

**Electronic supplementary material** The online version of this article (<https://doi.org/10.1007/s11144-018-1357-5>) contains supplementary material, which is available to authorized users.

✉ Faouzi Ayari  
faouzi.ayari@fst.utm.tn

<sup>1</sup> Laboratoire de Chimie des Matériaux et Catalyse, Faculté des Sciences de Tunis, Université de Tunis El Manar, Campus Universitaire Tunis El Manar, 2092 Tunis, Tunisia

<sup>2</sup> Faculté de Pharmacie de Monastir, Université de Monastir, Rue Avicenne, 5000 Monastir, Tunisia

<sup>3</sup> Dpto. Química Inorgánica y Química Técnica, Facultad de Ciencias, Universidad Nacional de Educación a Distancia, Paseo Senda del Rey 9, 28040 Madrid, Spain

<sup>4</sup> Institut Supérieur des Technologies Médicales de Tunis, Université de Tunis El Manar, 9 Avenue Docteur Zouhaier Essafi, 1006 Tunis, Tunisia

<sup>5</sup> Institut Charles Gerhardt Montpellier, UMR 5253, CNRS-UM-ENSCM, Matériaux Avancés pour la Catalyse et la Santé, ENSCM, 240 Avenue du Professeur Emile Jeanbrau, CS 60297, 34296 Montpellier Cedex 05, France

occupied the zeolite surface (46% of residual  $\text{MoO}_3$ ) and the internal cavities (9% of residual  $\text{MoO}_3$ ).

**Keywords** Molybdenum (VI) oxide · ZSM-5 · XPS · Gap energy

## Introduction

Molybdenum ( $_{42}\text{Mo}$ ) exchanged zeolites represent one of the technologically most important category of solid catalysts. In fact, they have been reported to catalyze phenanthrene hydrogenation [1], ethylene carbonylation [2], methyl–hydroxypentadecanoate macrolactonization [3], methane dehydroaromatization [4, 5],  $\text{C}_2\text{H}_x$  ( $x = 4$  and 6) ammoxidation [6], partial oxidation of *i*-butene [7], methanol conversion into gasoline [8], bitumen methanotreating [9], etc.

The most widely used method for the introduction of Mo into zeolites is the impregnation of the host structure with an ammonium heptamolybdate tetrahydrate solution [10, 11] followed by thermal treatments performed at different temperatures and extended for different time durations [12]. However, the introduction of molybdenum into zeolites by solid–state ion exchange (SSIE) is still a promising method [6, 11, 13]. Unfortunately, some authors [14, 15] pointed out that the SSIE of chlorinated Mo salts (e.g.  $\text{MoOCl}_4$  and  $\text{MoCl}_5$ ) into zeolites results in a substantial loss in crystallinity due to the attack by gaseous hydrogen chloride. Moreover, following the decomposition of ammonium heptamolybdate tetrahydrate under air [10], the diffusion of  $\text{MoO}_3$  crystallites into the ZSM-5 zeolite channels requires high temperatures ( $\sim 500$  °C), while the stabilization of Mo species with the framework oxygen occurs at 700 °C [10]. Such a stern thermal treatment would result in the extraction of Al ions from the framework with the subsequent formation of water and the disappearance of two Brönsted acid sites [16, 17]. Nonetheless, the solid–state ion exchange of organic precursors, e.g. Mo acetylacetonate, led to the formation of carbon at the surface of ZSM-5 zeolite, as covered by ourselves in a concise work [18], which shall not be reiterated here.

In the solid state, pure  $\text{MoO}_3$  is a suitable candidate for the introduction of Mo into ZSM-5 zeolite, and the studies dealing with the mechanistic aspects of solid–state ion exchange continue till date [19, 20]. Within the literature,  $\text{MoO}_3$  precursor is initially deposited on the external ZSM-5 surface and transformed to molybdenum *oxo* species, which are redistributed between the external surface and the internal channel structure [21]. Using Raman and X–ray absorption spectroscopies, Iglesia et al. [17, 22, 23] pointed out that the thermal activation of a physical mixture of  $\text{MoO}_3$  and ZSM-5 ( $\text{Si}/\text{Al} = 14.3$ ) under dry air results in the formation of  $(\text{MoO}_2(\text{OH}))^+$  species, which can condense with another identical moiety to form  $\text{H}_2\text{O}$  and  $(\text{Mo}_2\text{O}_5)^{2+}$  dimer, which bridges two Al framework sites. Moreover,  $(\text{MoO}_2(\text{OH}))^+$  species can also react with a zeolite OH group to form a  $(\text{MoO}_2)^{2+}$  cation bridging two acid sites and water. In 2006, Li et al. [24] mentioned the formation of  $\text{Mo}_5\text{O}_{12}^{6+}$  clusters upon the thermal treatment of ZSM-5 ( $\text{Si}/\text{Al} = 19$ ) and  $\text{MoO}_3$  under nitrogen stream between room temperature and 500 °C. Besides

these clusters, located at the ZSM-5 channel intersections, the X-ray diffraction (XRD) patterns revealed the presence of small  $\text{MoO}_3$  oxide particles on the external zeolite surface after calcination at 500 °C for 2 h [24]. Mosqueira et al. [25–27] placed particular emphasis on the thermal treatment of  $\text{MoO}_3$  in the presence of  $\gamma$ -alumina [25, 26], Y (Si/Al = 2.7) [25–27] and ZSM-5 (Si/Al = 37) [25, 26] zeolites at 450 °C under static air for different time durations (from 5 min to 24 h). These authors [25–27] have concluded that the migration of  $\text{MoO}_x$  species onto Y and ZSM-5 zeolites stabilized a significant fraction of tetrahedral Mo species (monomers and dimers) at the detriment of octahedral Mo heptamers. Specifically, the UV/visible diffuse reflectance spectroscopy (DRS) analysis revealed that the heptameric species were provided from the polymerization of Mo monomers over ZSM-5, while dimeric species were directly formed from  $\text{MoO}_3$  [26]. However, the thermal treatment of  $\text{MoO}_3$  in the presence of Y zeolite [27] led to the formation of  $\text{MoO}_2(\text{OH})_2$  volatile species which favoured the formation of monomers, firstly, then dimeric species, while Mo heptamers originated from the condensation of dimers.

The controversy in this literature overview is clear and the exact structure of Mo species stabilized on the zeolite is yet to be resolved. This work would contribute to the enlightenment and the enrichment of the points described in previous studies, dealing with the thermal activation of  $\text{MoO}_3$  and zeolite in the solid state. We have placed particular prominence on the interaction between  $\text{MoO}_3$  and  $\text{NH}_4^+$ -ZSM-5 (Si/Al = 26) under inert atmosphere using numerous characterization techniques.

## Experimental

### Preparation of $\text{MoO}_3/\text{NH}_4^+$ -ZSM-5 mixtures

The  $\text{MoO}_3$ /zeolite mixture was prepared by manually mixing the zeolite powder ( $\text{NH}_4^+$ -ZSM-5, Si/Al = 26, from Zeolyst) with the desired quantity (theoretical molar ratio Mo/Al = 1, i.e. 6 wt% of Mo and 9 wt% of  $\text{MoO}_3$ ) of  $\text{MoO}_3$  ( $M = 143.94 \text{ g mol}^{-1}$ , from Merck). The prepared mixture was divided into three equal fractions. Each fraction was treated under helium stream from room temperature to 500 °C ( $2 \text{ }^\circ\text{C min}^{-1}$ ) then kept isothermally at 500 °C for a particular length of time (this period was denoted as  $x$  and expressed in hours). The samples were labelled as  $\text{O}_x\text{-Z}$  ( $x$ ), i.e.  $\text{O}_x\text{-Z}$  (4 h),  $\text{O}_x\text{-Z}$  (8 h) and  $\text{O}_x\text{-Z}$  (12 h), where Z stands for the zeolite, while  $x$  is the duration of isothermal exchange at 500 °C (expressed in hours).

A reference sample was prepared by mixing  $\text{NH}_4^+$ -ZSM-5 with the desired quantity of  $\text{MoO}_3$  (6 wt% of Mo, i.e. 9 wt% of  $\text{MoO}_3$ ) and stored without undergoing thermal treatment. This reference material was labelled as  $\text{O}_x/\text{Z}$  (m.m.), where m.m. stands for mechanical mixture.

## Characterization

Thermal analysis curves were recorded under nitrogen flow (Air Liquide 99.998%, 30 mL min<sup>-1</sup>) from 30 to 800 °C (from 30 to 700 °C in the case of NH<sub>4</sub><sup>+</sup>-ZSM-5) with a 2 °C min<sup>-1</sup> heating rate using an SDT Q 600 apparatus. The outlet gases were simultaneously analyzed by a quadrupole mass spectrometer (Pfeiffer Vacuum, OmniStar™ GSD 301). The chemical analysis was performed by inductively coupled plasma–optical emission spectrometry (ICP–OES) on an Optima 3300 DV Perkin Elmer spectrometer. The morphology of the samples was studied by scanning electron microscopy (SEM) using a HITACHI 4800 S electron microscope, while the chemical composition was determined by energy dispersive X–ray (EDX). Textural analysis was performed by nitrogen physisorption at –196 °C on an automatic ASAP 2020 apparatus from Micromeritics. XRD measurements were performed on a Siemens D–500 diffractometer with CuK<sub>α</sub> radiation ( $\lambda = 1.54060 \text{ \AA}$ ), generator setting of 40 kV and 40 mA, a scanning speed of 0.2° min<sup>-1</sup> and a scanning region of 2–70°. X–ray photoelectron spectroscopy (XPS) spectra were recorded with an Omicron photoelectron spectrometer (MgK<sub>α</sub> = 1256 eV, 150 W, check supplementary material, page 7). Temperature programmed reduction under hydrogen (H<sub>2</sub>–TPR) was performed with a Micromeritics Autochem 2920 analyzer after a pretreatment under air flow (30 mL min<sup>-1</sup>) at 450 °C for 1 h. The sample was cooled and flushed with helium at room temperature before being reduced from 50 to 850 °C (or 750 °C) at a heating rate of 5 °C min<sup>-1</sup> with H<sub>2</sub> (3%)/Ar flow (30 mL min<sup>-1</sup>). Similarly to our previous works [6, 28–30], the TPR profiles were decomposed manually into Gaussian peaks using Origin 8.0 (Microcal Software, Inc., U.S.). Temperature programmed desorption of ammonia (NH<sub>3</sub>–TPD) analysis was performed with the same H<sub>2</sub>–TPR equipment. The sample was first exposed to air flow (30 mL min<sup>-1</sup>) at 450 °C for 1 h then saturated with flowing ammonia at 100 °C and flushed with helium at the same temperature. Finally, the temperature was ramped to 700 °C (10 °C min<sup>-1</sup>). UV–visible DRS spectra were recorded at room temperature on a Perkin Elmer Lambda 45 spectrophotometer. More details on the experimental protocol have been previously reported [6, 31].

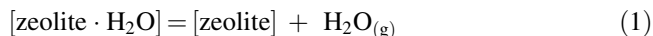
## Results

### Thermal analyses of NH<sub>4</sub><sup>+</sup>-ZSM-5, MoO<sub>3</sub> and Ox/Z (m.m.) samples

#### *Thermal analysis of NH<sub>4</sub><sup>+</sup>-ZSM-5*

Derivative thermogravimetric (DTG) and the mass spectrometry (MS) curves obtained during the thermal treatment of NH<sub>4</sub><sup>+</sup>-ZSM-5 zeolite (Si/Al = 26) under helium stream were previously presented in Ref. [18] and are reproduced in Fig. S1. The DTG curve (Fig. S1A) reveals the occurrence of different weight losses ascribed specifically to the dehydration and/or deammonization of the zeolite [18]. Interestingly, we noticed in Fig. S1B that the evolution of the signal intensity of

$\text{H}_2\text{O}^+$  MS fragment (blue-coloured curve, with a maximum at 30 °C) does not overlap with the weight loss interval situated between 30 and 170 °C in the DTG curve (Fig. S1A). According to Prilipko et al. [32], the shift of MS curve (relative to  $\text{H}_2\text{O}^+$ ) to the lower temperature region (in comparison with the DTG curve) is due to the fact that the reaction in Eq. 1 is displaced to the right.



The plots compiled in Fig. S1B indicate that gaseous ammonia (evacuated during the zeolite deammonization) is oxidized into  $\text{N}_2$  and  $\text{H}_2\text{O}$  at 420 °C as was reported earlier [15, 18, 33]. However, the moderate weight loss situated above 520 °C (yellow grid in Fig. S1A, inset) is attributed to the partial dehydroxylation of the zeolite [18].

### Thermal analyses of $\text{MoO}_3$ and Ox/Z (m.m.) samples

TG–DTG and derivative differential scanning calorimetry (deriv. DSC) curves recorded during the thermal treatment of pure  $\text{MoO}_{3(\text{s})}$  and  $\text{MoO}_3/\text{NH}_4^+$ –ZSM-5 mechanical mixture (i.e. Ox/Z (m.m.) sample) under helium stream are illustrated in Fig. 1. On the other hand, Figs. S2 and S3 represent the corresponding MS study results.

According to Fig. 1A, pure  $\text{MoO}_3$  oxide exhibits a dehydration process between room temperature and  $\sim 220$  °C with a weight loss of 5% (see the evolution of the signal intensity of  $\text{H}_2\text{O}^+$  MS fragment in Fig. S2A). In this context, Murugan et al. [34] investigated the thermal analysis of hydrated Mo oxide and noticed a deviation in the baselines at around 390 °C in both DTA and DSC thermograms. These authors [34] ascribed this deviation to the transformations between the polymorphic phases of  $\text{MoO}_3$  (Eq. 2).

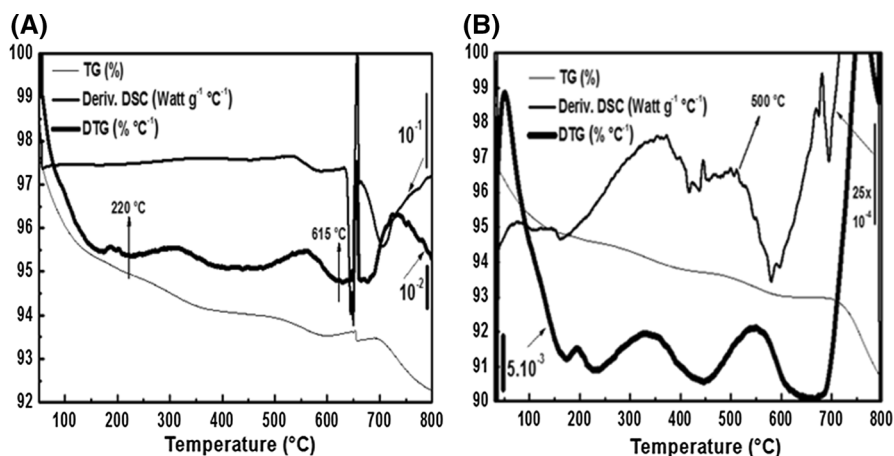
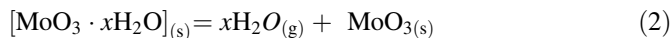


**Fig. 1** Thermal analysis curves of **A** pure  $\text{MoO}_3$  (from Merck), and **B**  $\text{MoO}_3/\text{NH}_4^+$ –ZSM-5 mechanical mixture (6 wt% of Mo) samples treated under helium stream ( $30 \text{ mL min}^{-1}$ ,  $2 \text{ °C min}^{-1}$ )



As a matter of fact, the ejected water molecules (Fig. S2A) would be initially present at the surface or inside the layers of Mo oxide and cannot originate from Eq. 2.

Following the dehydration of  $\text{MoO}_3$ , Fig. 1A revealed a weight loss of 1.42% between 220 and  $\sim 615$  °C, while Fig. S2B revealed the exit of oxygen. In their eminent work, Murugan et al. [34] reported that  $\text{MoO}_3$  is reduced into  $\text{MoO}_{3-\delta}$  above 400 °C (i.e. after the dehydration). Accordingly,  $\delta$  value was estimated in our study to be 0.13, in agreement with Murugan et al. results (i.e.  $0.09 < \delta < 0.25$  [34]).

The sudden weight loss observed at 650 °C in Fig. 1A would belong to the evaporation of  $\text{MoO}_3$  [18, 33] and probably  $\text{MoO}_{2.87}$  moiety.

In the case of Ox/Z (m.m.), Fig. 1B revealed four distinctive weight loss intervals. The first one, situated between room temperature and 220 °C, is related to the dehydration of both zeolite and salt (check the blue-colored curve in Fig. S3A). The second weight loss between 220 and 440 °C is associated with the desorption of ammonia (view the evolution of  $\text{NH}^+$  MS fragment in Fig. S3A) during zeolite deammonization. Between 440 and 650 °C, the observed weight loss would be associated with the exit of  $\text{H}_2\text{O}$  (Fig. S3A). However, above 650 °C,  $\text{MoO}_3$  is lost by evaporation as revealed by the drastic decrease in the TG curve intensity (Fig. 1B), while the zeolite dehydroxylation occurs above 700 °C as revealed by the evolution of the signal intensity of  $\text{H}_2\text{O}^+$  (pink gird in Fig. S3A).

It is worth to note that, throughout the 220–440 °C temperature range, the removal of water and oxygen is inhibited as confirmed by the evolution of  $\text{H}_2\text{O}^+$  and  $\text{O}^+$  signal intensities in Fig. S3A and Fig. S3B, respectively.

## Analysis of Ox–Z (x) mixtures treated isothermally at 500 °C

### Chemical analyses

The chemical analyses (ICP and EDX) results associated with  $\text{NH}_4^+$ –ZSM-5 zeolite and Ox–Z (12 h) solid are given in Table 1.

**Table 1** Chemical analysis results

Sample	Al (wt%)	Si/Al (mol/mol)	Mo (wt%)	Mo weigh loss (%) <sup>a</sup>	Mo <sup>b</sup> (wt%)
$\text{NH}_4^+$ –ZSM-5	1.30	27.01	–	–	–
Ox–Z (12 h)	1.33	25.05	3.67	38.80	8.51; 7.74; 6.22; 5.70; 4.93

<sup>a</sup>Defined as  $[(\text{Mo}_{\text{theoret}} - \text{Mo}_{\text{exper}})/\text{Mo}_{\text{theoret.}}] \times 100$

<sup>b</sup>Determined by EDX in five individual points at the surface

Considering the theoretical Mo content (6 wt%), the pronounced weight loss following 12 h of isothermal exchange at 500 °C (38.80%, Table 1) would come from the evaporation of molybdenum, probably in the form of  $\text{MoO}_2(\text{OH})_{2(g)}$ . In fact, the sublimation of  $\text{MoO}_3$  is not envisaged below 650 °C on the basis of our thermal analysis results (Fig. 1A) and based on Mosqueira et al. [26] results, which reported that residual  $\text{MoO}_3$  is still detected by XRD even after 24 h of thermal treatment at 450 °C.

In our study, despite the significant weight loss, molybdenum is well dispersed at the zeolite surface after 12 h of isothermal exchange as revealed by the EDX study results (average Mo wt% = 6.62, Table 1).

### SEM and nitrogen physisorption analyses

The micrographs of  $\text{NH}_4^+$ -ZSM-5 and Ox-Z (12 h) samples are illustrated in Fig. S5. According to the SEM images of Ox-Z (12 h) depicted in Fig. S5 (C and D), the shapes and the sizes (1 to 6  $\mu\text{m}$ ) of the zeolite crystals are similar to those observed in Fig. S5 (A and B). These results indicate that the solid-state ion exchange of Mo oxide does not affect the morphology of the zeolite crystals, even after 12 h of thermal treatment under helium stream at 500 °C.

The textural analysis results, expressed in terms of specific surface area ( $S_{\text{BET}}$ ), microporous and external areas ( $S_\mu$  and  $S_{\text{ext}}$ ), and (micro)porous volume(s) ( $V_\mu$  and  $V_p$ ), are compiled in Table 2.

Additionally, the theoretical dispersion capacity ( $W$ ) of  $\text{MoO}_3$  [35] inside the micropores of  $\text{NH}_4^+$ -ZSM-5 zeolite is included in Table 2. Considering the fact that the dynamic diameter of  $\text{MoO}_3$  is 5.0 Å [36, 37] and that the dimension of zeolite channel is 6 Å [35], it is therefore reasonable to believe that each  $\text{MoO}_3$  molecule could diffuse throughout the channels of  $\text{NH}_4^+$ -ZSM-5 and reach the internal cavities. Based on this postulation, the surface area occupied by each  $\text{MoO}_3$  molecule should be calculated by Eq. 3 [35].

$$A = \pi \times d \times l = 3.14 \times 6.0 \times 5.0 = 94.2 \text{ \AA}^2 \tag{3}$$

Here  $d$  stands for the diameter of the zeolite channel, while  $l$  represents the distance occupied by  $\text{MoO}_3$  in the channel and  $A$  is the surface area ( $\text{Å}^2$ ) occupied by each  $\text{MoO}_3$  molecule [35].

**Table 2** Textural properties and  $W$  values relative to the zeolite and Ox-Z ( $x$ ) solids: Effect of the exchange duration

Sample	$S_{\text{BET}}$ ( $\text{m}^2 \text{ g}^{-1}$ )	$S_\mu$ ( $\text{m}^2 \text{ g}^{-1}$ )	$S_{\text{ext}}$ ( $\text{m}^2 \text{ g}^{-1}$ )	$V_p$ ( $\text{mL g}^{-1}$ )	$V_\mu$ ( $\text{mL g}^{-1}$ )	$W$ (g)
$\text{NH}_4^+$ -ZSM-5	367	291	76	0.21	0.13	0.073
Ox-Z (4 h)	347	215	132	0.20	0.09	0.054
Ox-Z (8 h)	341	241	100	0.20	0.10	0.061
Ox-Z (12 h)	340	223	117	0.21	0.10	0.056

According to Table 2, the internal surface area of  $\text{NH}_4^+$ -ZSM-5 zeolite is  $291 \text{ m}^2 \text{ g}^{-1}$ . Therefore, the total number of  $\text{MoO}_3$  molecules dispersed inside the micropores of one gram of zeolite should be calculated by Eq. 4.

$$N = \frac{S_\mu}{A} = \frac{291}{94.2(\text{\AA}^2)} = 3.1 \times 10^{20} \quad (4)$$

Here  $S_\mu$  is the internal surface area of  $\text{NH}_4^+$ -ZSM-5 zeolite (Table 2) and  $N$  refers to the number of  $\text{MoO}_3$  molecules dispersed inside the micropores.

Taking into consideration Eqs. 3 and 4, the theoretical dispersion capacity ( $W$ ) of  $\text{MoO}_3$  inside the micropores of  $\text{NH}_4^+$ -ZSM-5 would be calculated by Eq. 5.

$$W = \frac{N}{6.023 \times 10^{23}} \times M_{\text{MoO}_3} = \frac{3.1 \times 10^{20}}{6.023 \times 10^{23}} \times 143.94 = 0.073 \text{ g} \quad (5)$$

In a similar way,  $W$  values were calculated in the case of Ox-Z (4 h), Ox-Z (8 h) and Ox-Z (12 h) solids (Table 2).

As reported in Table 2, the external area of  $\text{NH}_4^+$ -ZSM-5 zeolite exhibits a significant increase following 4 h of isothermal exchange at  $500^\circ\text{C}$ . Such an increase in  $S_{\text{ext}}$  value (from 76 to  $132 \text{ m}^2 \text{ g}^{-1}$ ) would be originated from the thermal treatment which might create some cracks, reduce the crystallites size and generate some meso/macroporosity following the exchange. Nevertheless, the SEM analysis results would exclude the massive cracking due to the similarity of the micrographs depicted in Fig. S5 (A and B) and S5 (C and D). Consequently, the change in the zeolite texture is ascribed to the presence of Mo.

The data compiled in Table 2 also revealed a pronounced decrease (26%) in the internal surface area of the zeolite following 4 h of isothermal exchange (i.e. Ox-Z (4 h) solid). This result indicates that  $\text{MoO}_3$  oxide diffuses throughout the internal cavities of the zeolite as there are no size restrictions (effectively,  $d = 6 \text{ \AA}$  and  $l = 5 \text{ \AA}$ ). However, in the case of Ox-Z (4 h) and Ox-Z (8 h) samples, the theoretical dispersion capacity values are 0.054 and 0.061 g. Seemingly, the increase in  $W$  values would indicate a pronounced diffusion of  $\text{MoO}_3$  throughout the micropores between 4 and 8 h. Nevertheless, for Ox-Z (4 h) and Ox-Z (12 h) solids, the similarity in  $W$  value ( $\sim 0.054 \text{ g}$ , which corresponds to the nominal  $\text{MoO}_3$  quantity (i.e.  $0.09 \times (100 - 38.80) \times 10^{-2}$ ) would discard the sublimation of  $\text{MoO}_3$  between 8 and 12 h of isothermal exchange.

## XRD

XRD patterns of pure  $\alpha$ - $\text{MoO}_3$  oxide and Ox-Z ( $x$ ) samples are illustrated in Fig. 2.

The XRD patterns of  $\text{MoO}_3/\text{NH}_4^+$ -ZSM-5 mixtures, illustrated in Fig. 2A, exhibits clear diffraction peaks at  $2\theta = 12.87, 25.78$  and  $39.10^\circ$ . Based on the XRD analysis performed with pure  $\text{MoO}_3$  (Fig. 2B), these peaks would correspond to crystalline  $\alpha$ - $\text{MoO}_3$  (020), (040) and (060) planes [38].

Using the Scherrer formula illustrated in Eq. 6 [39] and the main diffraction peak (Fig. 2B, inset), we were able to determine the size of  $\text{MoO}_3$  particles.



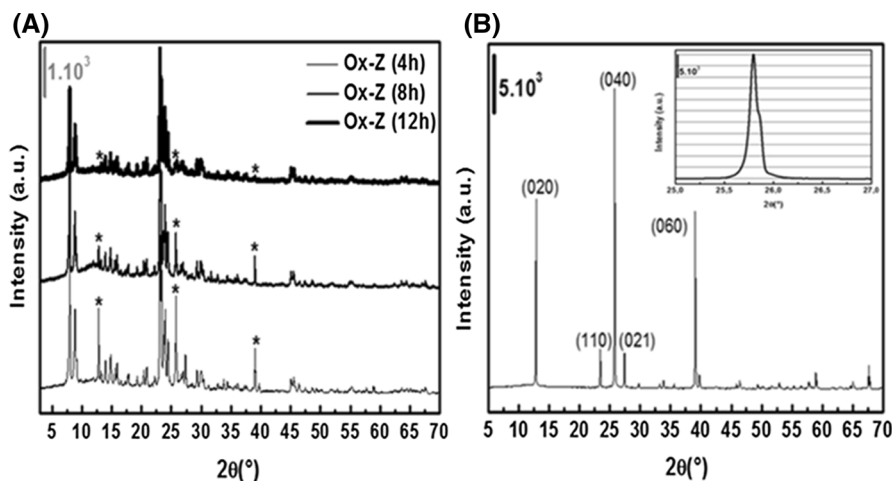


**Fig. 2** XRD patterns of **A** MoO<sub>3</sub>/NH<sub>4</sub><sup>+</sup>-ZSM-5 mechanical mixtures (6 wt% of Mo) treated from 30 to 500 °C (2 °C min<sup>-1</sup>) then isothermally at 500 °C for 4, 8 and 12 h under helium stream (30 mL min<sup>-1</sup>), and **B** pure α-MoO<sub>3</sub>. \*Crystalline α-MoO<sub>3</sub>

$$D \text{ (nm)} = 0.9 \times \lambda \times (\beta \times \cos \theta)^{-1} \tag{6}$$

Here *D* stands for the crystallite size,  $\lambda$  is the wavelength of the X-ray (0.154056 nm),  $\beta$  is the full width at half maximum (FWHM) of the Bragg peak (in radians) and  $\theta$  is the diffraction angle. The results are compiled in Table 3 and Fig. S6.

According to Table 3, the *D* values determined in the case of pure MoO<sub>3</sub> oxide and Ox-Z (4 h) solid do not differ significantly. However, *D* value increases from 68 to 114 nm between 4 and 8 h of isothermal exchange at 500 °C then decreases to 22 nm between 8 and 12 h. In line with these results, the agglomeration of MoO<sub>3</sub> particles at the surface (and therefore the increase in *D* value) would occur between 4 and 8 h of isothermal exchange at 500 °C. Nonetheless, extending the thermal treatment between 8 and 12 h reduces the crystallite size (from 114 to 22 nm) and increases the dispersion state of Mo (EDX results, Table 1).

### XPS

The Mo 3*d* XPS spectra of pure α-MoO<sub>3</sub> and Ox-Z (*x*) solids are illustrated in Figs. S7 and S8, while the quantitative study results are summarized in Table 4.

**Table 3** XRD results: MoO<sub>3</sub> crystallite size determined by the Scherrer’s formula

Sample	Bragg angle (°)	Size (nm)
(Pure MoO <sub>3</sub> )	25.78	77
Ox-Z (4 h)	25.75	68
Ox-Z (8 h)	25.73	114
Ox-Z (12 h)	25.76	22

**Table 4** XPS quantitative study results

Sample	$\alpha$ -MoO <sub>3</sub>	Ox-Z (4 h)	Ox-Z (8 h)	Ox-Z (12 h)
Mo 3d wt. conc. (%)	58.37	8.10	9.60	12.08
Al 2p wt. conc. (%)	–	3.83	5.01	3.88
Si 2p wt. conc. (%)	–	47.03	36.07	37.45
O 1s wt. conc. (%)	26.56	36.18	35.91	30.09
Bulk MoO <sub>3</sub> (at.%)	100	68	79	46
Oct./Tetr. Mo(VI) (at.%)	–	32	21	53

In the XPS spectrum of pure oxide (Fig. S7A), the core level binding energy peaks corresponding to 3d5/2 and 3d3/2 are observed at 234 and 237.2 eV, respectively [6, 40]. However, the XPS spectra of Ox-Z (*x*) solids (Fig. S7) undergo a broadening in the Mo 3d line shape, which could be attributed to the presence of more than one type of Mo<sup>6+</sup> specie [41]. The peak fitting analysis performed over the spectra of Ox-Z (4 h), Ox-Z (8 h) and Ox-Z (12 h) solids (check Fig. S8) revealed the presence of two additional components at ~ 232 and ~ 235 eV, which could be attributed to octahedral/tetrahedral Mo(VI) species [42]. In this context, Lede et al. [43] reported that molybdenum oxides may adopt different environments over ultrastable zeolite depending on the location of the anchoring site, being the tetrahedral structure, more or less distorted, is the most preserved one.

Interestingly, the XPS peak relative to bulk MoO<sub>3</sub> increases in intensity and undergoes a shift from 233.5 to 234 eV between 4 and 8 h of isothermal exchange at 500 °C (check red and magenta curves in Fig. S7C). These results corroborate the increase in the *D* values from 68 to 114 nm (Table 3) and confirm the agglomeration of MoO<sub>3</sub> oxide at the surface of Ox-Z (8 h) solid. However, between 8 and 12 h of isothermal exchange at 500 °C, the peak ascribed to bulk MoO<sub>3</sub> decreases in intensity (check wine and magenta curves in Fig. S7C) despite the increase in the Mo concentration at the surface (from 9.60 to 12.08%, Table 4). These results are in line with the decrease in *D* values between 8 and 12 h and agree with the fact that MoO<sub>3</sub> molecules do not diffuse throughout the micropores (check the decrease in *W* value from 0.061 to 0.056 g between 8 and 12 h of exchange, Table 2).

### H<sub>2</sub>-TPR

The TPR profiles of pure MoO<sub>3</sub> and Ox/Z (m.m.) samples are presented in Figs. S9 and S10. The shape of the TPR curves shows, at high temperatures, that the total reduction to Mo metal is not achieved at this stage. It is therefore possible that a small part of molybdenum species has not been reduced in the studied temperature range [44].

The TPR profile of pure MoO<sub>3</sub> (Fig. S9A) exhibits two main regions of hydrogen consumption. The first region situated below 783 °C is related to the reduction of

MoO<sub>3</sub> into MoO<sub>2</sub> [45]. However, the hydrogen consumption above 783 °C would correspond to the reduction of MoO<sub>2</sub> into metallic molybdenum [45, 46]. It is worth noting that the formation of Mo<sub>4</sub>O<sub>11</sub> intermediate during the reduction of MoO<sub>3</sub> into MoO<sub>2</sub> [46] is not excluded.

The peak fitting analysis performed over the TPR curve of Ox/Z (m.m.) sample (see Fig. S9B) revealed the presence of three peaks at 550, 585 and 640 °C. Given that a significant fraction of MoO<sub>3</sub> crystallites would occupy the external surface of the zeolite following the short TPR pretreatment (1 h at 450 °C), these peaks would correspond to the reduction of MoO<sub>3</sub> crystallites dispersed at the surface. However, the peaks situated at 710, 740, 800 and 840 °C in Fig. S9B would belong to the reduction of Mo<sub>4</sub>O<sub>11</sub> into MoO<sub>2</sub> or MoO<sub>2</sub> into metallic molybdenum [46].

Given that the reduction of the zeolite dehydroxylation-products and the evaporation of MoO<sub>2</sub> are not discarded, the deep interpretation of the high-temperature region should be avoided.

The peak fitting analyses performed over the TPR curves of Ox-Z (*x*) solids are presented in Fig. 3 (see also Fig. S10), while Table 5 compiles the quantitative study results.

The TPR profile of Ox-Z (4 h) solid exhibits four peaks at 480, 520, 540 and 575 °C (dashed lines in Fig. 3, check also Table 5) ascribed to the reduction of MoO<sub>3</sub> as will be later confirmed by XPS. However, the peaks at 350 and 440 °C (solid-lines) would correspond to the reduction of easy-reducible surface species other than MoO<sub>3</sub> oxide, while the peak at 730 °C (dotted line in Fig. 3) belongs to the reduction of MoO<sub>2</sub> into Mo (or Mo<sub>4</sub>O<sub>11</sub> into MoO<sub>2</sub> [46]). In the case of Ox-Z (8 h) solid, the easily reduced surface species exhibit three reduction peaks at 220, 310 and 385 °C (Table 5), while MoO<sub>3</sub> is reduced at 480 and 590 °C. For Ox-Z (12 h) solid, the reduction of MoO<sub>3</sub> occurs at 500 and 555 °C, while the peaks centred at 670, 810 and 840 °C (dotted-lines in Fig. 3) have been previously ascribed to the reduction of MoO<sub>2</sub> or Mo<sub>4</sub>O<sub>11</sub> [46]. Nevertheless, the peak centred at 610 °C would belong to the reduction of tetrahedral Mo<sup>6+</sup> species [6].

In order to verify the previous attribution of the reduction peaks, we calculated for each sample the percentage of MoO<sub>3</sub> using Eq. 7 (see more details in Table S1).

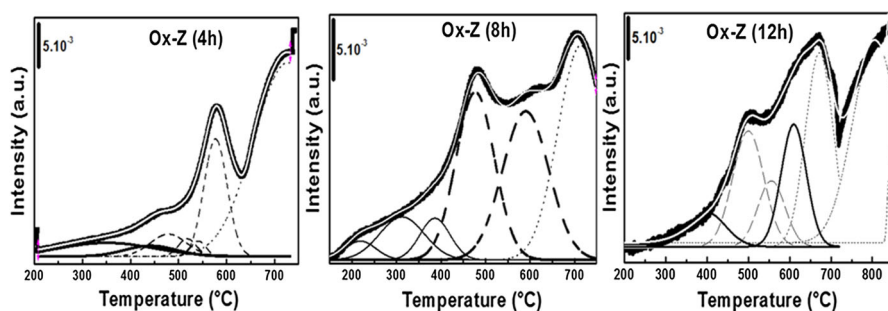


**Fig. 3** H<sub>2</sub>-TPR profiles of MoO<sub>3</sub>/NH<sub>4</sub><sup>+</sup>-ZSM-5 mechanical mixtures (6 wt% of Mo) treated from 30 to 500 °C (2 °C min<sup>-1</sup>) then isothermally at 500 °C for 4, 8 and 12 h under helium stream (30 mL min<sup>-1</sup>)

**Table 5** Reduction peaks and the corresponding areas

Sample	Peak maxima (°C) and the corresponding area ( <i>a.u.</i> )
Ox-Z (4 h)	350 (0.46)/440 (0.20)/480 (0.29)/520 (0.11)/540 (0.10)/575 (0.97)/730 (N.D.) <sup>a</sup>
Ox-Z (8 h)	220 (0.15)/310 (0.48)/385 (0.32)/480 (1.64)/590 (1.75)/715 (N.D.) <sup>a</sup>
Ox-Z (12 h) <sup>b</sup>	400 (0.50)/500 (1.40)/555 (0.70)/610 (1.20)/670 (N.D.) <sup>a</sup> /810 (N.D.) <sup>a</sup> /840 (N.D.) <sup>a</sup>

<sup>a</sup>Not determined<sup>b</sup>See Ref. [6]

$$\% \text{MoO}_3(\text{TPR}) = \frac{\text{areas of the peaks ascribed to MoO}_3}{\text{total area}} \quad (7)$$

It is worth noting that the dashed-line peaks in Fig. 3 correspond to the reduction of MoO<sub>3</sub>, while the total area is the sum of the areas under the dashed line and solid line peaks. In Fig. S11, we represented the percentage of MoO<sub>3</sub> determined by TPR versus its homologue determined by XPS. The linear plot presented in Fig. S11 corroborates the identification of reduction peaks, previously adopted.

### Optical spectroscopy study

In this study, we explored the absorption band gap using the Shuster–Kubelka–Munk function,  $F(R_\infty)$ , as given in Eqs. (8–10) [47].

$$F(R_\infty) = \frac{(1 - R^2)}{2R_\infty} = \frac{(hv - E_g)^n}{hv} \quad (8)$$

$$F(R_\infty) \times hv = (hv - E_g)^n \quad (9)$$

$$[F(R_\infty) \times hv]^{\frac{1}{n}} = hv - E_g \quad (10)$$

Here  $R_\infty$  is the diffuse reflectance of an infinitely thick sample,  $n$  is an exponent,  $hv$  is the photon energy and  $E_g$  is the optical energy gap of the material. The exponent  $n$  can take the values of 2, 3, 1/2 and 3/2 for indirect allowed, indirectly forbidden, directly allowed and directly forbidden transitions [47]. Plotting  $[F(R_\infty) \times hv]^{1/n}$  versus  $hv$  and extrapolating to  $[F(R_\infty) \times hv]^{1/n} = 0$  (in Eq. 10) yields the value of  $E_g$ .

In the case of MoO<sub>3</sub>, only  $n = 1/2$  (*i.e.* direct allowed transition) [26, 31, 48, 49] and  $n = 2$  (*i.e.* indirect allowed transition) [50–53] have been reported in the literature.

For pure MoO<sub>3</sub> and Ox/Z (m.m.) samples, the plots corresponding to either  $[F(R_\infty) \times hv]^2$  or  $[F(R_\infty) \times hv]^{0.5}$  versus  $hv$  are presented in Fig. 4. Additional functions, *i.e.*  $[F(R_\infty) \times hv]^{1/3}$  and  $[F(R_\infty) \times hv]^{2/3}$  versus  $hv$  were depicted in Figs. S12 and S13.

In the case of the direct allowed transition ( $n = 1/2$ ), *i.e.*, the plot representing  $[F(R_\infty) \times hv]^2$  vs.  $hv$  (Fig. 4A), we determined the area under the curve ascribed to

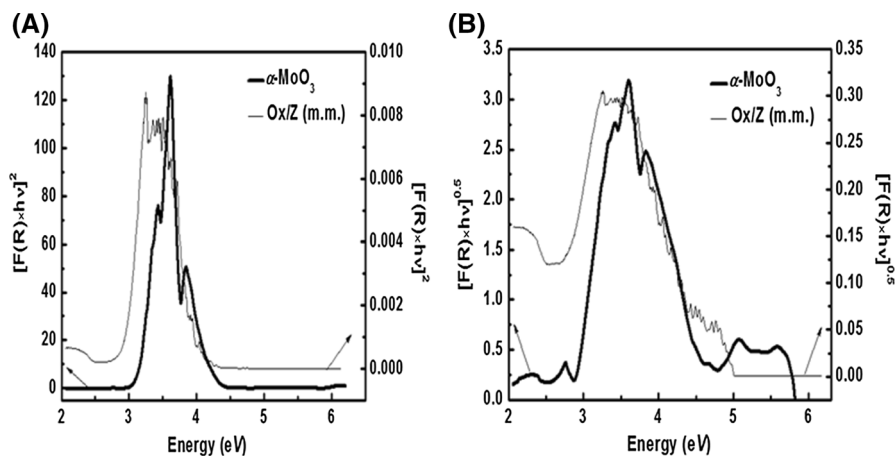
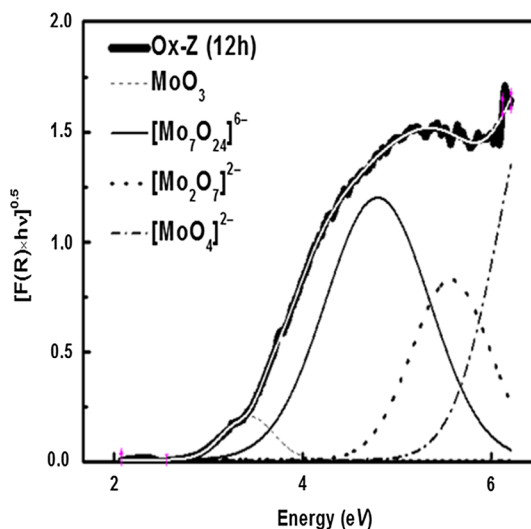


**Fig. 4** Optical absorption spectra of pure  $\text{MoO}_3$  and  $\text{MoO}_3/\text{NH}_4^+-\text{ZSM-5}$  fresh mechanical mixture (6 wt% of Mo, 9 wt% of  $\text{MoO}_3$ ): **A**  $[\text{F}(\text{R}_\infty) \times \text{h}\nu]^2$  versus  $\text{h}\nu$ , and **B**  $[\text{F}(\text{R}_\infty) \times \text{h}\nu]^{0.5}$  versus  $\text{h}\nu$  curves

Ox–Z (m.m.) to be 3.24 *a.u.*. However, the area under the curve attributed to pure  $\text{MoO}_3$  is 55.62 *a.u.*. The ratio of these areas (*i.e.* (3.24/55.62)  $\times$  100) does not correspond to the theoretical percentage of  $\text{MoO}_3$  in the mixture (*i.e.* 9%). In a similar way, and using the plots in Fig. 4B (representing the indirect allowed transition ( $n = 2$ , *i.e.*  $[\text{F}(\text{R}_\infty) \times \text{h}\nu]^{0.5}$  vs.  $\text{h}\nu$ ), the area ratio (*i.e.* (0.26/2.78)  $\times$  100) was calculated to be 9.4%, which is close to the theoretical  $\text{MoO}_3$  wt% in the mixture. Nevertheless, in the case of forbidden transitions (indirect transition for  $n = 3$  and direct transition for  $n = 3/2$ ), the area ratios for pure and diluted  $\text{MoO}_3$  do not correspond to 9% (Figs. S12 and S13). Consequently, it is concluded that the function  $[\text{F}(\text{R}_\infty) \times \text{h}\nu]^{0.5}$  satisfactorily describes our system.

**Fig. 5** UV absorption edges of  $\text{MoO}_3/\text{NH}_4^+-\text{ZSM-5}$  mechanical mixture (6 wt% of Mo, 9 wt% of  $\text{MoO}_3$ ) treated from 30 to 500  $^\circ\text{C}$  (2  $^\circ\text{C min}^{-1}$ ) then isothermally at 500  $^\circ\text{C}$  for 12 h under helium stream (30  $\text{mL min}^{-1}$ )



Figs. 5 and S14 represent the deconvolution of the DRS spectrum of Ox-Z (12 h) sample (see Ref. [31] for more details), while Table 6 summarizes the corresponding quantitative study results.

Based on the band gap analysis and the deconvolution of the spectrum relative to Ox-Z (12 h) solid, four  $O^{2-} \rightarrow Mo^{6+}$  charge transfer bands could be distinguished (Fig. 5). These ligand to metal charge transfer bands were assigned to  $MoO_3$  ( $E_g = 2.94$  eV),  $[Mo_7O_{24}]^{6-}$  ( $E_g = 3.65$  eV),  $[Mo_2O_7]^{2-}$  ( $E_g = 4.70$  eV) and  $[MoO_4]^{2-}$  ( $E_g = 5.56$  eV) [48]. However, despite the significant Mo weight loss (38.80%, Table 1) following 12 h of isothermal exchange at 500 °C, the area below the four bands in Fig. 5 (3.40 a.u.) exceeds the value obtained with pure and diluted  $MoO_3$  (2.78 and 0.26 a.u., Fig. 4B). This is predictable due to the fact that monomolybdate  $[MoO_4]^{2-}$ , dimolybdate  $[Mo_2O_7]^{2-}$  and heptamolybdate  $[Mo_7O_{24}]^{6-}$  species would exhibit different absorption coefficients (similarly to bare  $Co^{2+}$  ions [54] stabilized in BEA zeolite) and this is the reason for which we quantify only the  $MoO_3$  component.

Mosqueira et al. [26] identified different surface molybdate species over ZSM-5 zeolite by using DR measurements in the UV-visible region and carried out a band gap analysis of the deconvoluted spectra. Nevertheless, Mosqueira's study [26] only provides a semi-quantitative measure of the Mo *oxo*-species surface concentrations. Herein, we extrapolated our DRS measurements to a fully quantitative study by plotting the appropriate function (i.e.  $[F(R_\infty) \times hv]^{0.5}$ ).

## Discussion

The thermogravimetric analysis results (Figs. 1A, S2A and S4) revealed that unsupported  $MoO_3$  is dehydrated under helium stream between room temperature and 220 °C (weight loss = 5%). Similarly to Murugan's study [34], the desorbed water molecules do not evolve from the dehydration of  $MoO_3$  polymorphs (i.e. monoclinic  $MoO_3 \cdot 2H_2O$ , monoclinic and triclinic monohydrates ( $MoO_3 \cdot H_2O$ ), monoclinic hemihydrate ( $MoO_3 \cdot 0.5H_2O$ ) and orthorhombic  $MoO_3 \cdot 1/3 H_2O$  [55])

**Table 6** Edge energy values and  $MoO_3$  percentage

Sample	Edge energy ( $E_g$ ) values (eV)				
	$[MoO_4]^{2-}$	$[Mo_2O_7]^{2-}$	$[Mo_7O_{24}]^{6-}$	$MoO_3$	% of $MoO_3$
Pure $MoO_3$	–	–	–	2.88 (2.78) <sup>+</sup>	100
Ox-Z (m.m.)	–	–	–	2.54 (0.26) <sup>+</sup>	9.40 <sup>++</sup>
Ox-Z (12 h)	5.67*	4.73*	3.93*	3.30*	Not determined
	5.56**	4.70**	3.65**	2.94** (0.12) <sup>+</sup>	46 <sup>***</sup>

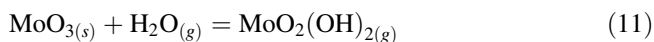
<sup>+</sup>Value between brackets: the area of  $MoO_3$  band in the curve  $[F(R_\infty) \times hv]^{0.5}$  versus  $hv$ , <sup>++</sup> Determined from Fig. 4 (i.e.  $(0.26/2.78) 100 = 9.4$ ), \* $E_g$  values obtained from the plot  $[F(R_\infty) \times hv]^2$  versus  $hv$  in Ref. [31], \*\* $E_g$  values obtained from the plot  $[F(R_\infty) \times hv]^{0.5}$  versus  $hv$  in this work (Fig. 5), \*\*\* $[0.12/0.26] \times 100$

given in Eq. (2) since we were not able to detect baseline deviations in our thermal analysis curves.

Following the dehydration, MoO<sub>3</sub> losses oxygen atoms (Fig. S2B) between 220 and 615 °C (weight loss = 1.42%) and transforms into MoO<sub>3-δ</sub> (δ = 0.13). However, at 650 °C, unreduced MoO<sub>3</sub> evaporates (Δ<sub>sub</sub>H = 276.56 kJ mol<sup>-1</sup>, Δ<sub>sub</sub>S = 300 J K<sup>-1</sup>mol<sup>-1</sup>, Δ<sub>sub</sub>G = - 3000 J mol<sup>-1</sup> [18]) as revealed by the sudden weight loss in Fig. 1A and by the derivative DSC curve in Fig. S4.

In the case of the mixture, the thermogravimetric analysis coupled to mass spectrometry (Figs. 1B and S3A) revealed that the dehydration takes place below 220 °C. However, gaseous ammonia evolved between 220 and 440 °C as revealed by the evolution of the signal intensity of NH<sup>+</sup> MS fragment (red curve in Fig. S3A). It is worth noting that the weight loss between 220 and 440 °C (0.84%, i.e. 0.5 mmol of NH<sub>3</sub> per gram, determined by NH<sub>3</sub>-TPD) is in agreement with the Al wt% determined by ICP-OES (Table 1). Therefore, we concluded that the dehydration of the mixture was inhibited between 220 and 440 °C (check also the blue curve in Fig. S3A).

Between 220 and 440 °C, H<sub>2</sub>O and MoO<sub>3</sub> were transformed into gaseous MoO<sub>2</sub>(OH)<sub>2</sub> according to Eq. 11.



It is a noticeable fact that, in this water-rich atmosphere, solid MoO<sub>3</sub> is not reduced into MoO<sub>3-δ'</sub> (δ ≠ δ') following the dehydration since the MS study results (Fig. S3B) excluded the formation of gaseous oxygen.

Between 440 and 600 °C, the non-isothermal ion exchange of the volatile MoO<sub>2</sub>(OH)<sub>2</sub> into H<sup>+</sup>-ZSM-5 is marked by the exit of H<sub>2</sub>O (Fig. S3A, grey gird) during the subsequent steps illustrated in Scheme S1. However, the exchange process, which involves the formation of H<sub>2</sub>O [18], is achieved at 500 °C as indicated by the decrease in both H<sub>2</sub>O<sup>+</sup> signal intensity (see the yellow arrow in Fig. S3A) and DSC signal in Figs. 1B and S4.

The partial dehydroxylation of the zeolite occurs at 520 °C (yellow gird in Fig. S1A inset), while MoO<sub>3</sub> evaporates at 650 °C. Accordingly, we performed the isothermal solid-state exchange of MoO<sub>3</sub> into ZSM-5 at 500 °C in order to avoid the zeolite dealumination and the loss of Mo.

Following 4 h of isothermal exchange at 500 °C (i.e. Ox-Z (4 h) solid), the theoretical dispersion capacity of MoO<sub>3</sub> (W) inside the zeolite micropores has been estimated to be 0.054 g (Table 2, last column). This theoretical value stands for the quantity of MoO<sub>3</sub> remaining after the weight loss (i.e. 0.09 g MoO<sub>3</sub> × (100 - 38.8) × 10<sup>-2</sup>). As a matter of fact, MoO<sub>2</sub>(OH)<sub>2</sub> is lost by evaporation between 220 and 440 °C since MoO<sub>3</sub> sublimates at 650 °C.

Between 4 and 8 h of isothermal exchange, the increase in W value (from 0.054 to 0.061 g) would ostensibly indicate the diffusion of MoO<sub>3</sub> inside the zeolite micropores. However, the similar W values for Ox-Z (4 h) and Ox-Z (12 h) solids would exclude the sublimation of MoO<sub>3</sub> between 8 and 12 h.

During the isothermal exchange between 4 and 8 h, we noticed the formation of MoO<sub>3</sub> agglomerates inside the zeolite bulk (revealed by the increase in D values

from 68 to 114 nm, Table 3) and at the surface (the increase in the bulk  $\text{MoO}_3$  percentage from 68 to 79%, Table 4, and in the  $\text{MoO}_3$  XPS peak intensity, Fig. S7C). However, between 8 and 12 h, the size of  $\text{MoO}_3$  crystallites decreased from 114 to 22 nm. In this context, we were able to exclude, on one hand, the diffusion of  $\text{MoO}_3$  inside the zeolite channels between 8 and 12 h (since  $W$  value decrease from 0.061 to 0.056 g) and the sublimation of  $\text{MoO}_3$  (similar  $W$  values for  $\text{Ox-Z}$  (4 h) and  $\text{Ox-Z}$  (12 h) solids) on the other hand. Seemingly, within this period (8–12 h),  $\text{MoO}_3$  is transformed into octahedral and tetrahedral  $\text{Mo(VI)}$  species at the surface, leading to the increase in Mo surface concentration (from 9.60 to 12.08%, Table 4) and the decrease in the  $\text{MoO}_3$  XPS peak intensity (Fig. S7C).

The identification of octahedral and tetrahedral  $\text{Mo(VI)}$  species was carried out by  $\text{H}_2$ -TPR. In effect, during the isothermal exchange at 500 °C for up to 4 h, gaseous  $\text{MoO}_2(\text{OH})_{2(g)}$  species were transformed into mono- and dimeric species according to the processes described in Scheme S1. However, these tetrahedral species, not yet stabilized at this stage, were transformed into heptamolybdates. According to the XPS study results, the concentration of heptamolybdate species at the surface of  $\text{Ox-Z}$  (4 h) solid is 32% (Table 4), and they were reduced under hydrogen at 350 and 440 °C (Fig. 3 and Table 5).

Between 4 and 8 h, mono- and dimolybdate species were not yet stabilized. Essentially, the  $\text{H}_2$ -TPR analysis of  $\text{Ox-Z}$  (8 h) solid (Fig. 3 and Table 5) revealed, on the one hand, the reduction of  $\text{MoO}_3$  agglomerates ( $D = 144$  nm) at 480 and 590 °C and heptaolybdate species at 220, 310 and 385 °C, on the other hand. Moreover, the decrease in the concentration of surface species (from 32 to 21%, Table 4) is due to the fact that a fraction of  $\text{MoO}_3$  diffuses inside the zeolite channels (increase in  $W$  value, Table 2) and is transformed into internal heptamolybdate species, inaccessible to the XPS beam.

Between 8 and 12 h, the concentration of  $\text{MoO}_3$  at the surface decreases from 79 to 46 at.%. At this stage, mono- and dimolybdates species were stabilized as revealed by the band gap analysis performed over  $\text{Ox-Z}$  (12 h) solid (Figs. 5 and S14). On the other hand, the  $\text{H}_2$ -TPR results evidenced the reduction of the monomolybdates at 610 °C (Fig. 3, Table 5). Concerning  $\text{MoO}_3$ , the percentages of residual oxide determined by DRS (Table 6) and XPS (Table 5) are similar (46%), while the value determined by TPR- $\text{H}_2$  is 55% (see Table S1). This result indicates that 9% of the total  $\text{MoO}_3$  occupied the internal channels, unable to be reached by the X-ray and UV beams.

In summary, the results of this study would exclude the formation of  $\text{Mo}_5\text{O}_{12}^{6+}$  clusters [24] (at least when using  $\text{NH}_4^+$ -ZSM-5, Si/Al = 26). However, until  $\text{MoO}_2(\text{OH})_2$  is not yet formed, the direct transformation of  $\text{MoO}_3$  into dimeric Mo is not envisaged. Seemingly,  $\text{MoO}_2(\text{OH})_2$  is condensed into polymolybdates in the first place and then into dimolybdates, while monomolybdates occupy, finally, the available sites.



## Conclusion

Unsupported  $\alpha$ -MoO<sub>3</sub> is dehydrated then reduced into MoO<sub>3- $\delta$</sub>  ( $\delta = 0.13$ ) between room temperature and 615 °C before being lost by sublimation at 650 °C. However, in the presence of the hydrated NH<sub>4</sub><sup>+</sup>-ZSM-5 zeolite (Si/Al = 26), the water molecules transformed a fraction of MoO<sub>3</sub> into gaseous MoO<sub>2</sub>(OH)<sub>2</sub> between 220 and 440 °C. During 4 h of isothermal exchange at 500 °C, gaseous MoO<sub>2</sub>(OH)<sub>2</sub> species reacted with the zeolite (already in its protonated form), leading to the formation of unstable mono- and dimeric species. The formed species were then transformed into surface heptamolybdates. However, between 4 and 8 h, residual MoO<sub>3</sub> is first agglomerated at the surface and then diffused throughout the internal cavities. The stabilization of monomolybdates and dimeric species in the cationic sites takes place within 8–12 h at 500 °C. Following 12 h of exchange we noticed that 55% of the total Mo occupied the zeolite surface and the micropores instead of being transformed into mono-, di- and polymeric species. In this study, the calculation of MoO<sub>3</sub> theoretical dispersion capacity improved the comprehension of the solid-state exchange of MoO<sub>3</sub> into ZSM-5 zeolite, while the DRS experiments were extrapolated to a fully-quantitative study using the  $[F(R_{\infty}) \times hv]^{0.5}$  function and a bunch of reference materials.

## References

1. Fu W, Zhang L, Wu D, Xiang M, Zhuo Q, Huang K, Tao Z, Tang T (2015) *J Catal* 330:423–433
2. Yang CC, Yacob S, Kilos BA, Barton DG, Weitz E, Notestein JM (2016) *J Catal* 338:313–320
3. Lai F, Liu X, Li W, Shen F (2010) *React Kinet Mech Catal* 100:407–415
4. Toosi MR, Sabour B, Hamuleh T, Peyrovi MH (2010) *React Kinet Mech Catal* 101:221–226
5. Kosinov N, Coumans FJAG, Uslamin EA, Wijpkema ASG, Mezari B, Hensen EJM (2017) *ACS Catal* 7:520–529
6. Mannei E, Ayari F, Petitto C, Asedegbega-Nieto E, Guerrero-Ruiz AR, Delahay G, Mhamdi M, Ghorbel A (2017) *Microporous Mesoporous Mater* 241:246–257
7. Corma A, Cortés Corberán V, Fornés V (1986) *React Kinet Catal Lett* 32:191–197
8. Zhu JH (1997) *React Kinet Catal Lett* 62:39–46
9. Zhao L, He P, Jarvis J, Song H (2016) *Energy Fuels* 30:10330–10340
10. Xu Y, Liu S, Guo X, Wang L, Xie M (1995) *Catal Lett* 30:135–149
11. Weckhuysen BM, Wang D, Rosynek MP, Lunsford JH (1998) *J Catal* 175:338–346
12. Ismagilov ZR, Matus EV, Tsikoza LT (2008) *Energy Environ Sci* 1:526–541
13. Li S, Zhang C, Kan Q, Wang D, Wu T, Lin L (1999) *Appl Catal A* 187:199–206
14. Dai PSE, Lunsford JH (1980) *J Catal* 64:173–183
15. Ayari F, Mannei E, Asedegbega-Nieto E, Mhamdi M, Guerrero-Ruiz AR, Delahay G, Ghorbel A (2017) *Thermochim Acta* 655:269–277
16. Liu W, Xu Y, Wong ST, Wang L, Qiu J, Yang N (1997) *J Mol Catal A* 120:257–265
17. Borry RW III, Kim YH, Huffsmith A, Reimer JA, Iglesia E (1999) *J Phys Chem B* 103:5787–5796
18. Mannei E, Ayari F, Asedegbega-Nieto E, Mhamdi M, Guerrero-Ruiz AR, Delahay G, Ghorbel A (2017) *Thermochim Acta* 652:150–159
19. Zhang Z, Zhang Q, Jia L, Wang W, Gao X, Gu Y, Gao X, Han Y, Tan Y (2016) *Chem Sel* 1:6127–6135
20. Kosinov N, Coumans FJAG, Li G, Uslamin E, Mezari B, Wijpkema ASG, Pidko EA, Hensen EJM (2017) *J Catal* 346:125–133

21. Burns S, Hargreaves JSJ, Stockenhuber M, Wells RPK (2007) *Microporous Mesoporous Mater* 104:97–102
22. Li W, Meitzner D, Borry RW III, Iglesia E (2000) *J Catal* 191:373–383
23. Lacheen HS, Iglesia E (2005) *Phys Chem Chem Phys* 7:538–547
24. Li B, Li S, Li N, Chen H, Zhang W, Bao X, Lin B (2006) *Microporous Mesoporous Mater* 88:244–253
25. Mosqueira L, Fuentes GA (2002) *Mol Phys* 100:3055–3057
26. Mosqueira L, Gómez SA, Fuentes GA (2004) *J Phys* 16:S2319–S2327
27. Mosqueira L, Angeles-Chavez C, Torres-García E (2011) *Mater Chem Phys* 126:930–937
28. Ayari F, Mhamdi M, Delahay G, Ghorbel A (2009) *J Sol Gel Sci Technol* 49:170–179
29. Ayari F, Mhamdi M, Debecker DP, Gaigneaux EM, Álvarez-Rodríguez J, Guerrero-Ruiz AR, Delahay G, Ghorbel A (2011) *J Mol Catal A* 339:8–16
30. Ayari F, Mhamdi M, Alvarez-Rodríguez J, Guerrero-Ruiz AR, Delahay G, Ghorbel A (2013) *Appl Catal B* 134–135:367–380
31. Mannei E, Ayari F, Mhamdi M, Almohalla M, Guerrero Ruiz AR, Delahay G, Ghorbel A (2016) *Microporous Mesoporous Mater* 219:77–86
32. Prilipko AI, Il'in VG, Turutina NV, Nazarenko VA, Mel'nichenko GN (1990) *Theor Exp Chem* 25:467–470
33. Ayari F, Mannei E, Asedegbega-Nieto E, Mhamdi M, Guerrero-Ruiz AR, Delahay G, Ghorbel A (2017) *J Therm Anal Calorim*. <https://doi.org/10.1007/s10973-017-6545-4>
34. Murugan P, Ghule A, Bhongale C, Chang H (2000) *J Mater Chem* 10:2157–2162
35. Xiao FS, Zheng S, Sun J, Yu R, Qiu S, Xu R (1998) *J Catal* 176:474–487
36. Wells AF (1975) *Structural inorganic chemistry*, 4th edn. Oxford University Press, London
37. Shriver DF, Atkins PW, Langford CH (1990) *Inorganic chemistry*. Freeman, New York
38. JCPDS data file No 05–0508
39. Patterson AL (1939) *Phys Rev* 56:978–982
40. Hussain OH, Rao KS (2003) *Mater Chem Phys* 80:638–646
41. Zingg DS, Makovsky LE, Tischer RE, Brown FR, Hercules DM (1980) *J Phys Chem* 84:2898–2913
42. Naumkin AV, Vass AK, Gaarenstroom SW, Powell CJ (2012) XPS database, NIST Standard Reference Database 20, Version 4.1, 2012
43. Lede EJ, Requejo FG, Pawelec B, Fierro JLG (2002) *J Phys Chem B* 106:7824–7831
44. Arnoldy P, Franken MC, Scheffer B, Moulijn JA (1985) *J Catal* 96:381–395
45. Arnoldy P, de Jonge JCM, Moulijn JA (1985) *J Phys Chem* 89:4517–4526
46. Bhaskar T, Reddy KR, Kumar CP, Murthy MRVS, Chary KVR (2001) *Appl Catal A* 211:189–201
47. Khan GA, Hogarth CA (1991) *J Mater Sci* 26:412–416
48. Weber RS (1995) *J Catal* 151:470–474
49. Braun S, Appel LG, Schmal M (2002) *Appl Surf Sci* 201:227–235
50. Anwar M, Hogarth CA (1988) *Phys Stat Sol A* 109:469–478
51. Donnadiou A, Davazoglou D, Abdellaoui A (1988) *Thin Solid Films* 164:333–338
52. Anwar M, Hogarth CA (1989) *J Mater Sci* 24:3673–3678
53. Chithambararaj A, Sanjini NS, Velmathi S, Chandra Bose A (2013) *Phys Chem Chem Phys* 15:14761–14769
54. Essid S, Ayari F, Bulánek R, Vaculík J, Mhamdi M, Delahay G, Ghorbel A (2017) *Catal Today*. <https://doi.org/10.1016/j.cattod.2017.08.027>
55. Seguin L, Figlarz M, Cavagnat R, Lassègues JC (1995) *Spectrochim Acta Part A* 51:1323–1344